

An X-ray Raman spectrometer for EXAFS studies on minerals: bent Laue spectrometer with 20 keV X-rays

N. Hiraoka,^{a*} H. Fukui,^b H. Tanida,^c H. Toyokawa,^c Y. Q. Cai^d and K. D. Tsuei^a

^aNational Synchrotron Radiation Research Center, Hsinchu 30076, Taiwan, ^bGraduate School of Material Science, University of Hyogo, 3-2-1 Kouto, Kamigori, Hyogo 679-1297, Japan, ^cJapan Synchrotron Radiation Research Institute, 1-1-1 Kouto, Sayo, Hyogo 679-5198, Japan, and ^dPhoton Sciences, Brookhaven National Laboratory, Upton, NY 11973-5000, USA.
E-mail: hiraoka@spring8.or.jp

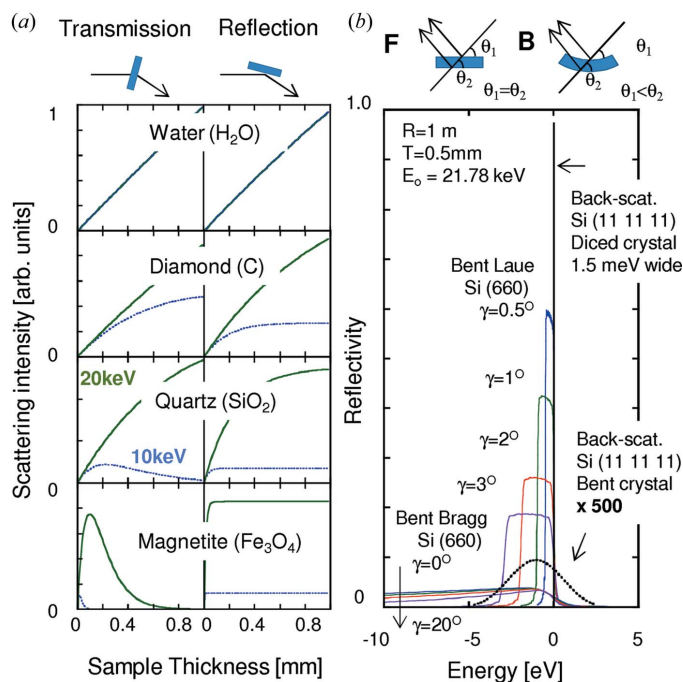
An X-ray Raman spectrometer for studies of local structures in minerals is discussed. Contrary to widely adopted back-scattering spectrometers using ≤ 10 keV X-rays, a spectrometer utilizing ~ 20 keV X-rays and a bent Laue analyzer is proposed. The 20 keV photons penetrate mineral samples much more deeply than 10 keV photons, so that high intensity is obtained owing to an enhancement of the scattering volume. Furthermore, a bent Laue analyzer provides a wide band-pass and a high reflectivity, leading to a much enhanced integrated intensity. A prototype spectrometer has been constructed and performance tests carried out. The oxygen *K*-edge in SiO₂ glass and crystal (α -quartz) has been measured with energy resolutions of 4 eV (EXAFS mode) and 1.3 eV (XANES mode). Unlike methods previously adopted, it is proposed to determine the pre-edge curve based on a theoretical Compton profile and a Monte Carlo multiple-scattering simulation before extracting EXAFS features. It is shown that the obtained EXAFS features are reproduced fairly well by a cluster model with a minimal set of fitting parameters. The spectrometer and the data processing proposed here are readily applicable to high-pressure studies.

1. Introduction

X-ray absorption spectroscopy (XAS) is widely used as a tool for investigating local electronic and atomic structures in a sample. In particular, the extended X-ray absorption fine structure (EXAFS) carries much information for elucidating the local structure of liquid and glass. However, it is not trivial to apply this method to compounds consisting of light elements, such as silicate minerals. This is because for elements lighter than Si their absorption edges are only in the soft X-ray region, which poses various restrictions on the sample environment, including the need for ultrahigh vacuum and the high surface sensitivity. These restrictions prevent studies under extreme conditions such as high pressure. X-ray Raman scattering (XRS) can overcome these problems. In XRS, an absorption edge is probed as a function of an energy loss between the incident photon and the scattered photon, but the incident photon energy can be chosen arbitrarily. Therefore if hard X-rays are used as the incident photon, the restrictions on the sample environment can be largely relaxed. Nonetheless, the intensity is substantially weaker owing to the small scattering cross section, making the practical application

difficult. While there are many successful examples of X-ray absorption near-edge structure (XANES)-type XRS studies, those of EXAFS-type are not so many because very high statistical accuracies are necessary for the latter. After demonstration work on graphite and diamond by Tohji & Udagawa (1987, 1989), several XRS-EXAFS experiments were performed (Bowron *et al.*, 2000; Fister *et al.*, 2006a; Bergmann *et al.*, 2007; Huotari *et al.*, 2012). In those experiments, samples as thick as several millimetres were measured to compensate for the small scattering cross section, except for the measurement on Mg and Al foils by Fister *et al.* (2006a).

Fig. 1(a) plots the scattering intensities from several minerals as a function of the sample thickness. It is clear that the volume enhancement, *i.e.* the intensity enhancement by increasing the scattering volume, is effective on very low-*Z* samples for 10 keV X-rays. However, it drastically becomes less effective if the sample contains elements with a slightly higher *Z* value such as Si, Al or further heavier elements such as Fe. The scattering volume is determined by the penetration depth rather than the sample thickness, and for 10 keV X-rays the penetration depth is only ~ 100 μm or even smaller for these samples. Furthermore, if a high-pressure experiment is


Figure 1

(a) Scattering intensities as a function of the sample thickness in transmission (Laue) and reflection (Bragg) geometry. (b) Reflectivity curves of bent (B) and flat (or diced) (F) analyzers at 21.78 keV.

considered, such a small penetration depth makes it more difficult because a weak signal from a tiny sample can be easily veiled by other scattering from the high-pressure cell. These facts often hamper the XRS studies, particularly XRS-EXAFS studies, on minerals under high-pressure conditions.

Use of higher-energy X-rays, *e.g.* of 20 keV, would easily solve the problem because they have a much larger penetration depth. However, the solution is not so straightforward. Presently, most of the XRS spectrometers adopt the back-scattering geometry with spherical analyzers (see, for example, Cai *et al.*, 2004; Huotari *et al.*, 2005; Fister *et al.*, 2006*b*; Verbeni *et al.*, 2009; Gog *et al.*, 2009). As described below, the so-called Darwin width of the back-scattering analyzer rapidly decreases as the X-ray energy increases from 10 keV to 20 keV, leading to a substantial drop of the reflectance. This is a favourable trend in terms of the resolution (as is indeed utilized in high-resolution phonon measurements by inelastic X-ray scattering) but an unfavourable mismatch for XRS. For most of the XRS measurements, particularly EXAFS-type studies, such a high resolution is not necessary, while the intensity is the most critical for improving the statistical accuracy of the experiment.

In this report we discuss an X-ray Raman spectrometer for EXAFS studies on minerals. Using a bent Laue analyzer with 20 keV X-rays, we have constructed a prototype and tested the performance. Energy resolutions of 4 eV (EXAFS mode) and 1.3 eV (XANES mode) have been achieved. EXAFS features are extracted in the post-edge region of the oxygen *K*-edge in SiO₂ glass and crystal, and are compared with a theoretical model. Note that the goal of the present spectrometer is different from that of commercially available bent-crystal

Laue analyzers, developed for fluorescence XAS. Our goal is to measure an inelastic spectrum with an energy resolution one or two orders of magnitude higher than that of fluorescence XAS.

2. Bent Laue analyzer for 20 keV X-rays

Fig. 1(b) shows the reflectivity curves of analyzers in the back-scattering geometry (Si 11 11 11 reflection, $\theta_B = 87^\circ$) and in the forward-scattering geometry (Si 660, $\theta_B = 26^\circ$), which the multi-lamellar model provides (Erola *et al.*, 1990).¹ If a spherical diced analyzer is used around 20 keV (Masciovecchio *et al.*, 1996), the reflection has to be high-index such as (11 11 11). The Darwin width of such a high-index reflection is significantly narrower [see the thick solid line in Fig. 1(b)] with a small integrated reflectivity, compared with the required energy resolution of an XRS experiment (~ 1 eV). This is the reason why such diced spherical analyzers are not suitable to XRS. On the other hand, a continuously bent analyzer has a much wider band-pass because the lattice parameter varies owing to a stain in the curved crystal and also because the diffraction plane gradually tilts as the beam penetrates into the crystal [see the diagram in Fig. 1(b)]. However, the back-scattering bent analyzer does not work well in this energy region: the peak reflectivity is very low and thus the integrated reflectivity is also small [thick dotted line in Fig. 1(b)]. This is because the thickness of each lamellar (layer), determined by the Darwin width, is much smaller than the extinction length for such a high-index reflection (Erola *et al.*, 1990). In contrast, the reflectivity curve of the bent Laue analyzer is excellent and well suited for XRS [thin solid lines in Fig. 1(b)]. In particular, it is a great advantage that the band-pass is adjustable by introducing a small amount of the asymmetric angle, γ (or modifying the crystal thickness). Note that, for a bent Bragg analyzer in the forward-scattering geometry, such properties are attainable only in the limit $\gamma \rightarrow 90^\circ$, so it provides a too wide band-pass with a very small peak reflectivity in a practical γ -range.

The disadvantage of the bent Laue analyzer is that it is difficult to achieve a high energy resolution, as expressed by $\Delta E = (E/\tan\theta_B)\Delta\theta$, where θ_B is the Bragg angle, always small in the forward-scattering geometry. $\Delta\theta$ is the incident beam divergence due, for example, to a finite beam size on the sample and/or the slope error of the analyzer. The energy resolution is therefore critically influenced by the beam size at the sample position and the slope error of the analyzer.

3. Performance test

The spectrometer was tested at the Taiwan inelastic X-ray scattering beamline BL12XU at SPring-8, Japan. Fig. 2(a) shows the main optical components of the beamline. The synchro-

¹ We have checked the consistency between our code and the widely used *XOP* code. The latter provides a higher peak reflectivity (as much as double in some cases), while the width is the same, probably due to a different calculation manner for the absorption. However, such a difference does not affect the present conclusion.

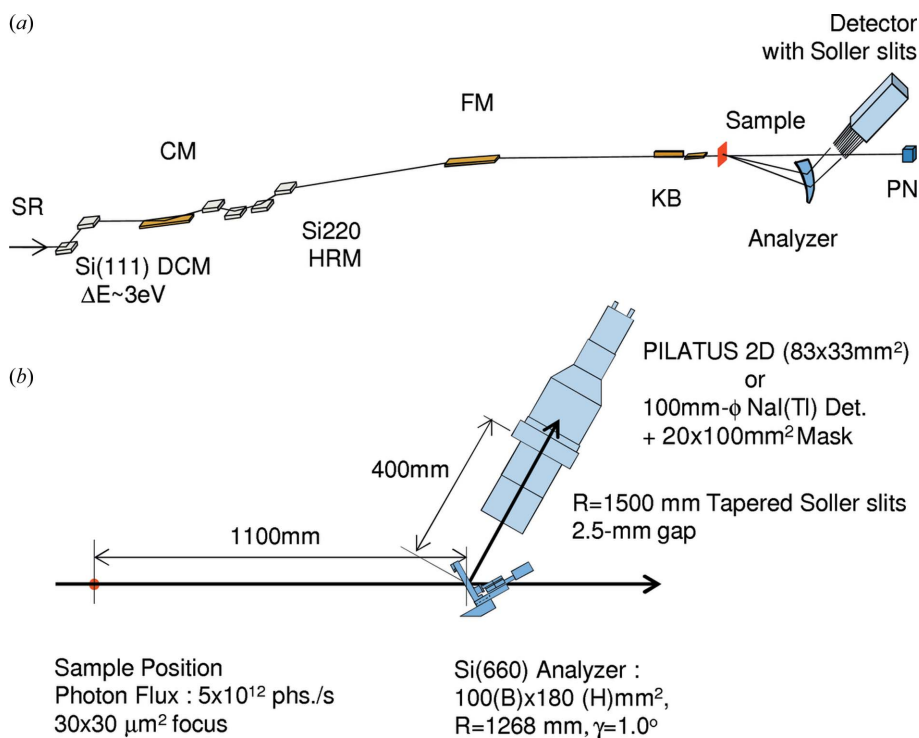


Figure 2
 (a) Layout of beamline BL12XU/SP8. DCM, double-crystal monochromator; CM, collimating mirror; HRM, channel-cut high-resolution monochromator; FM, focusing mirror; KB, Kirkpatrick–Baez mirror. Mirrors are all Pt-coated. PN indicates a Si PIN diode for beam monitoring. (b) Sketch of the bent Laue spectrometer.

tron radiation from an undulator source (third harmonics) was monochromated by a Si 111 double-crystal monochromator (DCM) with an energy width of 3 eV at 19.5 keV. For an XANES measurement requiring a higher energy resolution, we inserted four-bounce Si 220 channel-cut crystals after the DCM. The beam was then focused by Pt mirrors into a $30 \mu\text{m} \times 30 \mu\text{m}$ spot. The available flux was 5×10^{12} photons s^{-1} in the EXAFS mode ($\Delta E \simeq 3\text{eV}$) and 1×10^{12} photons s^{-1} in the XANES mode ($\Delta E \simeq 0.8\text{eV}$). Higher-order radiation contamination is negligibly small because the beam was reflected four times by the Pt-coated mirrors having a reflectivity of $\leq 0.5\%$ each at 58.5 or 97.5 keV, assuming a 2.5 mrad incidence and a 0.5 nm root-mean-square (r.m.s.) roughness. (Actual incidence angles were even larger, leading to a lower reflectivity.) The analyzer and a detector were mounted in such a way that the scattering plane was horizontal while the Rowland circle (*i.e.* the dispersion plane of the analyzer) was vertical. In this geometry the energy resolution is independent of the penetration depth and most of the scattered photons are σ -polarized. These are important in maximizing the intensity in the forward-scattering geometry. The beam intensity was monitored by a Si PIN diode before or after the sample.

Fig. 2(b) shows a sketch of the spectrometer. Scattered X-rays are diffracted by Si 660 planes ($\theta_B = 29.8^\circ$ at 19.5 keV) in a cylindrically bent analyzer with a radius of 1.28 m. The crystal has a triangular shape with 100 mm base and 180 mm height, and has a thickness of 0.5 mm. The [001] axis is (almost) normal to the triangular surface. The asymmetric

angle has been optimized to 1.0° in terms of the bandwidth and the reflectivity, aiming at an approximately 1 eV resolution (more precisely, 1.3 eV resolution, which is most often chosen with a 10 keV set-up for XRS). We have tested two types of detectors. One is a PILATUS two-dimensional detector having a $83.8\text{ mm} \times 33.5\text{ mm}$ active area with pixels of $172 \mu\text{m} \times 172 \mu\text{m}$ each. The sensor is made of 450 μm -thick Si, leading to an absorbance of 38%. The Laue analyzer is cylindrically bent and thus the divergence along the horizontal (sagittal) axis is not compensated. Furthermore, it is not easy to achieve a uniform curvature over a wide region. The two-dimensional detector corrects those well as shown below. The other detector is a large-area (100 mm-diameter) scintillation counter having a mask of $100\text{ mm} \times 20\text{ mm}$ (V \times H) in front. The scintillator is a 3 mm-thick NaI(Tl) crystal having an $\sim 100\%$ efficiency. This is the so-called point detector, correcting neither the slope error nor the divergence, but a sufficient energy resolution is still available for EXAFS measurements. A pair of

tapered Soller slits (horizontal and vertical) are placed in front of these detectors. They are made of stainless steel plates having poor surfaces (to avoid the total reflection) with a gap of 2.5 mm. They are very effective in reducing the background.

3.1. Resolution function

Fig. 3 shows spectra of the elastic and inelastic scattering from 1 mm-thick SiO_2 glass. The resolution is evaluated to be 1.7 eV (XANES mode) and 4.0 eV (EXAFS mode) from the width of the elastic line (right inset in Fig. 3). The Si 220 channel-cut crystals were installed after the Si 111 DCM in the XANES mode. The NaI detector was used in both cases. Fig. 4(a) shows how the profile of the elastic scattering varies as a function of the position on the analyzer. They were measured by scanning a mask of aperture $5\text{ mm} \times 5\text{ mm}$ before the analyzer. The elastic line shifts to higher energy and becomes broader away from the centre of the analyzer. The shift along the horizontal axis is not avoidable for the cylindrically bent analyzer as mentioned already, while that along the vertical axis arises from the slope error. The two-dimensional detector perfectly corrects them. Fig. 4(b) displays the principle of the correction and an example. We measured the profiles of the elastic line by dividing the active area into 50 regions before measuring the inelastic parts, so as to find a peak position in energy at each division. We then measured the oxygen *K*-edge in α -quartz along the [001] axis. Again we took the 50 inelastic spectra and summed them up by

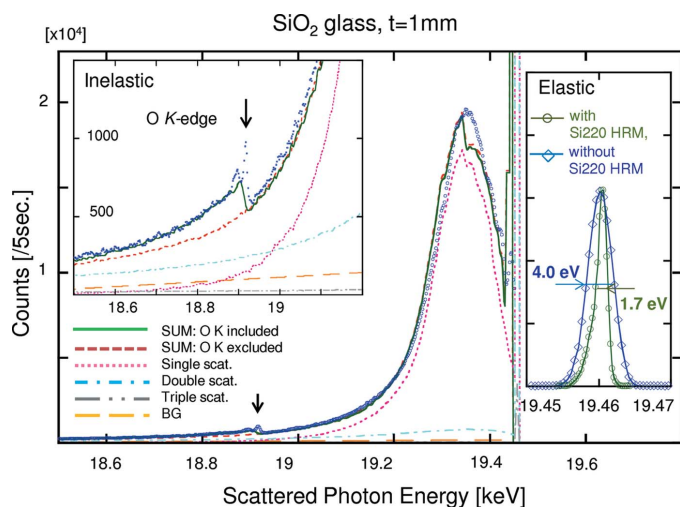


Figure 3 Experimental XRS spectrum (dotted line), compared with Monte Carlo multiple-scattering simulation including (solid line) and excluding (broken line) the O *K*-edge. Single, double and triple scattering components are shown as well as a linear background. The inset on the right shows elastic scattering profiles with (circles) and without (diamonds) the Si 220 high-resolution monochromator.

considering the peak shifts of the elastic energy, so that the slope error as well as the horizontal divergence was all corrected. The lower panel in Fig. 4(b) displays a corrected *K*-edge feature, which exhibits well resolved features at 542 and 547 eV, being characteristic of quartz (Lin *et al.*, 2007; Lee *et al.*, 2008; Fukui *et al.*, 2008). The resolution function is given by the line profile of the elastic scattering after summing with the same amounts of the energy shifts. [Note that the uncorrected elastic profile in Fig. 4(b) is wider than in Fig. 3 because the

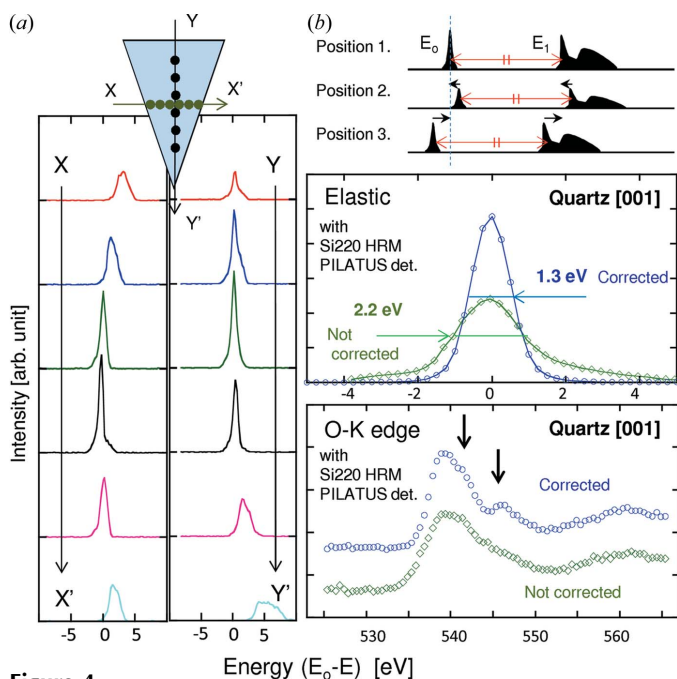


Figure 4 (a) Profile of elastic scattering as a function of position on the analyzer. (b) Example of the energy shift correction by the two-dimensional detector. Arrows indicate features characteristic of quartz.

active area is larger.] The problematic tail is dramatically suppressed while the peak intensity is enhanced. The final resolution is evaluated to be 1.3 eV from the full width at half-maximum of the elastic scattering profile.

3.2. XRS-EXAFS

EXAFS is an oscillating structure in a wide energy range of the post-edge region. The biggest concern in extracting EXAFS information from an XRS spectrum is that there is no established way to determine the pre-edge curve. Some empirical methods such as a polynomial fitting used to be carried out in early studies but this becomes quite arbitrary away from the absorption edge. Sternemann *et al.* (2008) proposed a more precise method for a subtraction but we attempt here another approach. As seen in Fig. 3, an inelastic spectrum is generally dominated by Compton scattering while edge features are small peaks on it. Therefore, we first need to know the general trend of the Compton profile. A theoretical Compton profile can be obtained by band theory² and their multiple-scattering events can be simulated by a Monte Carlo simulation (Fajardo *et al.*, 1998). Data-processing here is almost equivalent to that in previous reports (Bergmann *et al.*, 2007; Sternemann *et al.*, 2008; Huotari *et al.*, 2012) but a notable difference is the evaluation of multiple-scattering events of photons. Note that the multiple-scattering mentioned here is for photons making a smooth background while the one often argued in the previous reports is for electrons making the oscillation features. As seen in Fig. 3, double scattering events have a significant contribution around the O *K*-edge. This correction becomes more important with increasing energy or increasing penetration depth of the photons. The overall shape of the inelastic spectrum is then reproduced well as seen in Fig. 3, and the simulated spectrum is now a good reference to determine the pre-edge curve and/or post-edge curve. At the end, we still have to rely on fitting with analytic functions, *e.g.* exponential decays, to obtain a smooth curve but we have a solid reference over a wide energy range of the post-edge region.

Fig. 5(a) shows the XRS spectra of the O *K*-edge in SiO₂ crystal and glass, measured with a 4 eV resolution. The scattering angle is 30°. In a one-day exposure, 50000 counts have been accumulated at the white peak before the pre-edge curve subtraction while 30000 counts were accumulated after the subtraction (*i.e.* 30000 counts for the edge jump). The counting rate is ~200 counts s⁻¹, which is ~15 times higher than that in the existing 10 keV set-up with a single back-scattering analyzer of radius 2 m.³ The post-edge curves have been

² The valence electron contributions were computed based on the local density approximation by the code *BANDS*, which was available at BL08W, SPring-8, while the contributions of core electrons in each shell, read from the table by Biggs *et al.* (1975), were summed considering the cut-off at their absorption edges.

³ The analyzer is a Si 555 spherically bent analyzer having a mask of diameter 85 mm in front. Our code provides a reflectivity curve like an asymmetric Gaussian having a tail to the lower energy side once a Si 555 Bragg crystal is assumed to be cylindrically bent with a 2 m radius. The peak intensity is 40% while the width is 100 meV (FWHM). We expect that the spherical crystal has a lower peak and a wider width owing to a larger strain.

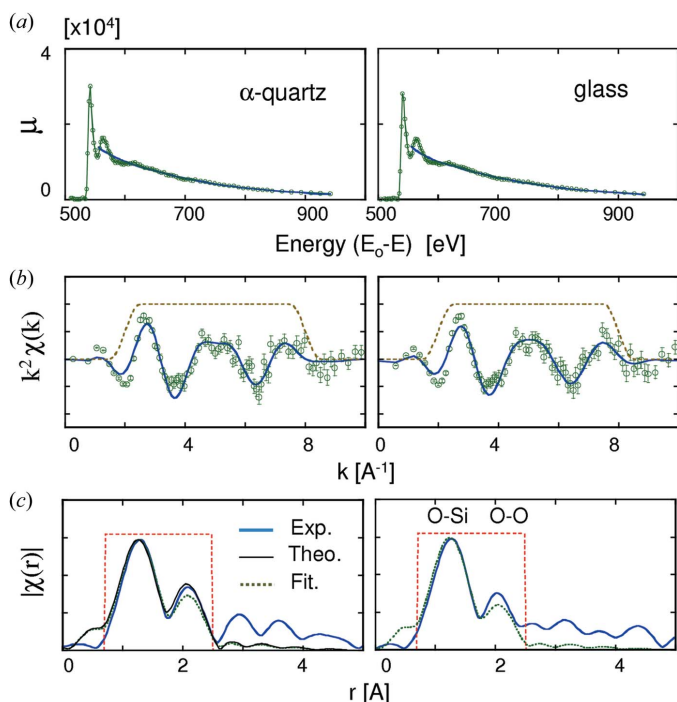


Figure 5
 (a) XRS spectra after subtraction of the pre-edge curve, (b) $\chi(k)$ weighted by k^2 and (c) $\chi(r)$ along with fitted curves. The solid curves in (b) are $k^2\chi(k)$ by backward Fourier transformation of $\chi(r)$ in the 0.8–2.5 Å r -range. The thin curve in (c) is $\chi(r)$ by theory with an adjustment of peak height while dotted curves are by four-parameter fitting. Broken curves in (b) and (c) are window functions in forward and backward Fourier transformations.

determined by a spline fitting as in usual XAS (Ravel & Newville, 2005).⁴ Fig. 5(b) displays $\chi(k)$ after the subtraction of the post-edge curves while Fig. 5(c) shows $\chi(r)$ by their Fourier transformation in the 2–8 Å⁻¹ k -range. The solid lines overlaid in Fig. 5(b) are obtained by the backward Fourier transformation of $\chi(r)$ in the 0.8–2.5 Å r -range. The $\chi(k)$ are weighted by k^2 rather than k and k^3 . We have found that k provides a considerably broader $\chi(r)$ while k^3 leads to too much influence from statistical errors. It is inevitable for XRS to have larger statistical error-bars compared with XAS. Nonetheless, it is clearly seen in Fig. 5 that there are consistent oscillation features in the crystal and the glass. This is a reasonable finding because it is widely believed that they have similar local structures at ambient pressure. We have attempted a fitting analysis based on a cluster model. The models were constructed based on the crystal structure of α -quartz. We first tested a minimal parameter fitting on the quartz, where a Debye–Waller factor is fixed so that the peak height at 1.3 Å is identical to that of the experiment [see the thin curve in Fig. 5(c)]. They show a fairly good agreement. Another fitting was made with four parameters: an isotropic expansion parameter (α), related to effective distances (r_{eff}) for Si–O and O–O, two Debye–Waller factors (σ^2) and an energy shift (ΔE). Again they show reasonable agreements

⁴ *ATHENA* code was used to obtain $\chi(k)$ and $\chi(r)$ while *ARTEMIS* code was used for a model fitting. See Ravel & Newville (2005) for details.

Table 1

Theoretical (fixed) parameters used for a comparison with experiment: coordination numbers (N), averaged effective distances (r_{eff}), Debye–Waller factors (σ^2) and energy shifts (ΔE).

σ^2 is adjusted so that maximum height is identical with experiment.

	N	r_{eff} (Å)	σ^2 (Å ²)	ΔE (eV)
Quartz				
O–Si	2	1.605	0.0105	0
O–O	6	2.622	0.0105	0

Table 2

Resultant parameters after fitting analysis.

Fitting parameters are the isotropic expansion coefficient (α), related to r_{eff} , the Debye–Waller factor (σ^2) for O–Si and O–O, and the energy shift (ΔE)

	N	r_{eff} (Å)	σ^2 (Å ²)	ΔE (eV)
Quartz				
O–Si	2	1.61 (± 0.03)	0.0099 (± 0.0028)	0.99 (± 3.57)
O–O	6	2.63 (± 0.03)	0.0152 (± 0.0075)	0.99 (± 3.57)
Glass				
O–Si	2	1.59 (± 0.04)	0.0098 (± 0.0028)	0.21 (± 4.13)
O–O	6	2.59 (± 0.06)	0.0201 (± 0.0075)	0.21 (± 4.13)

(dotted curves). The results are tabulated in Tables 1 and 2. These (perhaps surprising) agreements indicate (i) that one can extract information of local structures by XRS-EXAFS despite their poorer statistical accuracies than XAS-EXAFS, and (ii) that one can have consistent results even though the data process originally developed for XAS is applied to XRS.

Finally, we briefly discuss the non-dipolar transition contribution. Although the dipole approximation is not strictly satisfied in our case ($q \cdot r \simeq 0.5$), the previous reports indicate that the non-dipolar contribution is quite small and only provides a minor modification (Bergmann *et al.*, 2007; Huotari *et al.*, 2012). Huotari *et al.* showed this was because the $L = 0$ and $L = 2$ non-dipolar transitions, showing relatively large intensities, were in anti-phase with each other and thus they were mostly cancelled out. The fact that a standard EXAFS procedure works well here re-confirms that the oscillation features are dominated by the dipolar components.

4. Conclusion and prospects

We propose a bent Laue spectrometer with ~20 keV X-rays for studies of local structures in minerals such as silicates. We have constructed a prototype spectrometer and tested its performance. The achieved energy resolutions are 4 eV (EXAFS mode) and 1.3 eV (XANES mode). The two-dimensional detector corrects the slope errors of the analyzer well. In the EXAFS mode of the present set-up the counting rate on SiO₂ glass is 200 counts s⁻¹ at the O K -edge: this is about 15 times higher than that in the existing 10 keV back-scattering set-up with a single 2 m-radius analyzer. The solid angle detecting the scattered photons is similar, 8.8×10^{-4} sr for the former while 10.4×10^{-4} sr for the latter. The 10 keV spectrometer is equipped with multi-analyzer systems (nine analyzers at most) while the present 20 keV spectrometers

have only one analyzer. Therefore, the improvement factors are reduced to ~ 5 and 2.5, compared with the three-analyzer set-up (most often used) and the nine-analyzer set-up, respectively. (The ratio is not proportional to the number of analyzers because of the non-uniform performance.) The introduction of multi-analyzers is our next plan. It is also important to increase the detection efficiency of a two-dimensional detector: this would enhance the count rate by a factor of ≥ 2 .

Our primary goal is to study local structures in trinary compounds or minerals. Conventional XAS and electron spectroscopy are impossible under high pressure while the interpretation of a radial distribution function from X-ray diffraction rapidly becomes difficult as the number of elements increases. The application of the present spectrometer to high-pressure experiment is straightforward and existing techniques are readily applicable (Hiraoka & Cai, 2010). Indeed, we have measured the EXAFS features in magnesium silicate glass up to 11.5 GPa and a higher pressure measurement is in progress. Recently developed pressure cells with polycrystalline or sintered diamond anvils having a large culet can compress a relatively large sample volume, for example of 0.7 mm diameter and 0.1 mm thickness, up to several tens of GPa (Okuchi *et al.*, 2012). The bent Laue spectrometer will greatly benefit from such a large anvil cell.

Another interesting application is in an *L*- or *M*-edge XANES study on iron-based minerals under pressure. The high-spin to low-spin transition in Fe ions is often argued to be important in the earth's formation process (Nomura *et al.*, 2011). Fe *L*- and *M*-edge XANES is much more sensitive to the spin-transition than *K*-edge XANES. This is one of the most difficult experiments with a 10 keV spectrometer because the absorption is high and thus a sample has to be very small, so that the signal is easily masked by other scattering from the anvils or the gasket, but this is quite performable with the 20 keV spectrometer. We have already obtained a good quality preliminary result.

We thank Veijo Honkimäki (ESRF) for providing us with a code calculating the reflectivity of a bent crystal. We are grateful to Kenji Ishii (JAEA) for his help in operation of the PILATUS detector. The experiment was performed under approval of JASRI (No. 2008B4258) and NSRRC, Taiwan (No. 2008-3-071-6). YQC is supported by the US Department of Energy, Office Basic Energy Science, under Contract No. DE-AC02-98CH10886.

References

- Bergmann, U., Di Cicco, A., Wernet, P., Principi, E., Glatzel, P. & Nilsson, A. (2007). *J. Chem. Phys.* **127**, 174504.
- Biggs, F., Mendelsohn, L. B. & Mann, J. B. (1975). *At. Data Nucl. Data Tables*, **16**, 201–309.
- Bowron, D. T., Krisch, M. H., Barnes, A. C., Finney, J. L., Kaprolat, A. & Lorenzen, M. (2000). *Phys. Rev. B*, **62**, R9223–R9227.
- Cai, Y. Q., Chow, P., Chen, C. C., Ishii, H., Tsang, K. L., Kao, C. C., Liang, K. S. & Chen, C. T. (2004). *AIP Conf. Proc.* **705**, 340–343.
- Erola, E., Eteläniemi, V., Suortti, P., Pattison, P. & Thomlinson, W. (1990). *J. Appl. Cryst.* **23**, 35–42.
- Fajardo, P., Honkimäki, V., Buslaps, T. & Sourtti, P. (1998). *Nucl. Instrum. Methods Phys. Res. B*, **134**, 337–345.
- Fister, T. T., Seidler, G. T., Hamner, C., Cross, J. O., Soinenen, J. A. & Rehr, J. J. (2006a). *Phys. Rev. B*, **74**, 214117.
- Fister, T. T., Seidler, G. T., Wharton, L., Battle, A. R., Ellis, T. B., Cross, J. O., Macrander, A. T., Elam, W. T., Tyson, T. A. & Qian, Q. (2006b). *Rev. Sci. Instrum.* **77**, 063901.
- Fukui, H., Kanzaki, M., Hiraoka, N. & Cai, Y. Q. (2008). *Phys. Rev. B*, **78**, 012203.
- Gog, T., Seidler, G. T., Casa, D. M., Upton, M. H., Kim, J., Stoupin, S., Nagle, K. P., Balasubramanian, M., Gordon, R. A., Fister, T. T., Heald, S. M., Toellner, T., Hill, J. P., Coburn, D. S., Kim, Y. J., Said, A. H., Alp, E. E., Sturhahn, W., Yavas, H., Burns, C. A. & Sinn, H. (2009). *Synchrotron Radiat. News*, **22**, 12–21.
- Hiraoka, N. & Cai, Y. Q. (2010). *Synchrotron Radiat. News*, **23**, 26–31.
- Huotari, S., Pylkkänen, T., Soinenen, J. A., Kas, J. J., Hämäläinen, K. & Monaco, G. (2012). *J. Synchrotron Rad.* **19**, 106–113.
- Huotari, S., Vankó, Gy., Albergamo, F., Ponchut, C., Graafsma, H., Henriquet, C., Verbeni, R. & Monaco, G. (2005). *J. Synchrotron Rad.* **12**, 467–472.
- Lee, S. K., Lin, J. F., Cai, Y. Q., Hiraoka, N., Eng, P. J., Okuchi, T., Mao, H. K., Meng, Y., Hu, M. Y., Chow, P., Shu, J., Li, B., Fukui, H., Lee, B. H., Kim, H. N. & Yoo, C. S. (2008). *Proc. Nat. Acad. Sci.* **105**, 7925–7929.
- Lin, J. F., Fukui, H., Prendergast, D., Okuchi, T., Cai, Y. Q., Hiraoka, N., Yoo, C. S., Trave, A., Eng, P., Hu, M. Y. & Chow, P. (2007). *Phys. Rev. B*, **75**, 012201.
- Masciovecchio, C., Bergmann, U., Krisch, M., Ruocco, G., Sette, F. & Verbeni, R. (1996). *Nucl. Instrum. Methods Phys. Res. B*, **111**, 181–186.
- Nomura, R., Ozawa, H., Tateno, S., Hirose, K., Hernlund, J., Muto, S., Ishii, H. & Hiraoka, N. (2011). *Nature (London)*, **473**, 199–202.
- Okuchi, T., Sasaki, S., Ohno, Y., Abe, J., Arima, H., Osakabe, T., Hattori, T., Sano-Furukawa, A., Komatsu, K., Kagi, H., Utsumi, W., Harjo, S., Ito, T. & Aizawa, K. (2012). *J. Phys. Conf. Ser.* **377**, 012013.
- Ravel, B. & Newville, M. (2005). *J. Synchrotron Rad.* **12**, 537–541.
- Sternemann, H., Sternemann, C., Seidler, G. T., Fister, T. T., Sakko, A. & Tolan, M. (2008). *J. Synchrotron Rad.* **15**, 162–169.
- Thoji, K. & Udagawa, Y. (1987). *Phys. Rev. B*, **36**, R9410–R9412.
- Thoji, K. & Udagawa, Y. (1989). *Phys. Rev. B*, **39**, 7590–7594.
- Verbeni, R., Pylkkänen, T., Huotari, S., Simonelli, L., Vankó, G., Martel, K., Henriquet, C. & Monaco, G. (2009). *J. Synchrotron Rad.* **16**, 469–476.